Molecular-weight dependence of morphology and mechanical properties of hydroxypropyl cellulose films cast from water

Masaru Matsuo* and Naoko Yanagida
Department of Clothing Science, Faculty of Home Economics, Nara Women's University, Nara 630, Japan
(Received 3 April 1990; revised 11 May 1990; accepted 20 August 1990)

The morphology and mechanical properties of hydroxypropyl cellulose films cast from water were investigated in terms of molecular-weight dependence using sample with three molecular weights. The maximum draw ratio increased with molecular weight. The Young's modulus decreased with temperature, while the crystal lattice modulus was independent of temperature. This difference was thought to be due to thermal expansion of the average distance between amorphous chain segments. The experimental and theoretical aspects of the molecular-weight dependence of morphology were mainly studied by small-angle light scattering. The theoretical calculation was carried out by considering the interparticle interference effects of rods.

(Keywords: hydroxypropyl cellulose; molecular-weight dependence; maximum draw ratio; crystal lattice modulus; small-angle light scattering)

INTRODUCTION

It is well known that hydroxypropyl cellulose (HPC) is a water-soluble derivative of native cellulose[1,2] that is composed of a backbone of anhydroglucose units, permitting the formation of poly(1,2-alkyleneoxy) side chains. Extensive work has been reported by Samuels[1] on the orientation of both crystalline and amorphous regions as well as on the deformation of the superstructure in the process of strain-induced crystallization. The morphological properties were investigated at all levels from molecular to superstructural by X-ray diffraction, small-angle light scattering, birefringence and infra-red measurements. According to his report[1], the HPC molecule has a cellulosic backbone of anhydroglucose units twisted into an irregular 3_1 helix and there exist three anhydroglucose units per 15 Å repeat. He pointed out that intramolecular hydrogen bonding of the poly(propylene oxide) side chains leads to a stiff rod-like molecule and these molecules are packed into microfibrillar crystallites 470 Å long and 34 Å in diameter. On the basis of his results, this paper deals with the morphology and mechanical properties of HPC films with different molecular weights, in order to study whether the drawability of HPC film depends on molecular weight.

The improvement of the mechanical properties of a film (or fibre) has been studied by using polyethylene from the viewpoint that the attainable draw ratio depends on the number of entanglements per molecule. Smith and Lemstra succeeded in producing high-modulus fibres using the gel deformation method[3-5] to solve the problem that the attainable draw ratio of melt-crystallized polyethylene decreases with increasing molecular weight. A dry gel film with high drawability was produced by crystallization from dilute solution using polyethylene with molecular weight greater than 10^6. This phenomenon is attributed to a reduced number of entanglements per molecule in solution-cast/spun polymers in comparison with those obtained from the melt. Another method was developed by Ward[6,7] and Porter[8] to produce high-modulus film (or fibre) using low-molecular-weight polyethylene. Their concept is basically identical to that of gel deformation[9]. Since a melt film has a number of entanglements intrinsically, low-molecular-weight polyethylene plays an important role to restrain a drastic increase in entanglement meshes with molecular weight, in order to assure a suitable level of entanglement meshes for transmitting the drawing force effectively.

Unfortunately, no report exists giving detailed information about drawability of HPC. Through a number of experiments, it was found that water or ethanol must be used as the solvent to assure transparency of the resultant film, but these solvents do not allow an HPC gel film to form at room temperature. Accordingly, water is used as the solvent to obtain a cast film in this experiment. Molecular orientation was estimated by X-ray diffraction and birefringence measurements, and the mechanical properties were discussed in relation to molecular orientation. Furthermore, the crystal lattice modulus of HPC was measured as a function of temperature by X-ray diffraction.

The deformation of superstructures is studied by means of small-angle light scattering under Hv polarization conditions. It is an objective of this experiment to

* To whom correspondence should be addressed

0032-3861/91/142561-16

investigate the deformation of rods, the optical axis being fixed at 45° with respect to the rod axis in an undeformed state. In this analysis, a model is proposed to calculate Hv light scattering patterns by considering the interparticle interference effect of rods.

EXPERIMENTAL

Three kinds of HPC powders with different molecular weights were used as test specimens. The viscosities were measured in ethanol by an Ubbelohde-type capillary viscometer. The characteristics of the three kinds of HPC specimens are listed in *Table 1*. The substitution of HPC is expressed in terms of the molar substitution (*MS*). The values of the weight-average molecular weight $\bar{M}_w$ and the number-average molecular weight $\bar{M}_n$ were estimated by using gel permeation. Their values were measured by Dr S. Sudo of Yamagata University.

HPC films were prepared by casting on a flat plate from solutions of concentration 10 g/100 ml for specimens A and B and 2.5 g/100 ml for specimen C, with subsequent air drying at room temperature. The resultant films, which had a thickness of about 150 μm, were vacuum dried for 1 day to remove residual traces of solvent.

The dry film was cut into strips of length 70 mm and width 10 mm. The strips were clamped in a manual device in such a way that the length to be drawn was 50 mm. The specimen was placed in a hot oven at 170°C under nitrogen and elongated manually to the desired draw ratio after annealing for 15 min. After stretching, the stretcher with the sample was annealed at 170°C for 10 min and cooled slowly to room temperature.

The density of the films was measured in a pycnometer with n-heptane and carbon tetrachloride as the medium. The degree of crystallinity was calculated by assuming the densities of the crystal and amorphous regions to be 2.0548 and 1.088 g cm^{-3}, respectively[1].

The thermal behaviour was estimated using differential scanning calorimetry (d.s.c.) curves. Samples, weighing 5 mg, were placed in a standard aluminium sample pan. The samples were heated at a constant rate of 10°C min^{-1}.

The X-ray measurements were carried out using a 12 kW rotating-anode X-ray generator (RDA-rA). WAXD patterns were obtained with a flat-film camera using Cu K_α radiation at 200 mA and 40 kV. The X-ray beam was monochromatized by a curved graphite monochromator. The exposure time for all specimens was 1 h, when the incident beam was directed parallel to the film surface (end view) and along the film normal direction (through view). SAXS patterns were obtained with a flat-film camera. The exposure time for all the specimens was 100 h in the case of through and end views.

Birefringence measurements were made in a polarizing microscope using a Berek compensator to measure the retardation.

Table 1 Characterization of three kinds of HPC specimens

HPC	*MS*	$\bar{M}_w$ ($\times 10^4$)	$\bar{M}_n$ ($\times 10^4$)
Specimen A	4.25	11.7	5.2
Specimen B	3.48	19.2	8.9
Specimen C	3.37	119.5	26.8

Light scattering patterns were obtained with a 3 mW He–Ne gas laser as the light source. Diffuse surfaces were avoided by sandwiching the specimen between microcover glasses with a silicone immersion oil having a similar index of refraction.

The complex dynamic tensile modulus functions were measured at a frequency of 10 Hz over the temperature range from −50°C to the breaking point of each specimen using a viscoelastic spectrometer (VES-F) obtained from Iwamoto Machine Co. Ltd. The length of the specimen between the jaws was about 40 mm and the width about 1.5 mm. During measurements, the film was subjected to a static tensile strain in order to place the sample in tension during the axial sinusoidal oscillation, which had a peak deformation of 0.2%. The complex dynamic modulus was measured by imposing a small dynamic strain to assure linear viscoelastic behaviour of the specimen[10].

Crystal strain was provided by a constant-stretching apparatus that has been described elsewhere[11,12]. The specimen was mounted horizontally in the stretching clamps and examined by X-ray diffraction. The intensity distribution from the (0 0 2) plane was measured with point focusing by using a system in which the incident beam was collimated by a circular collimator 2 mm in diameter, and the diffracted beam was detected by a square slit with dimensions 0.9 mm × 0.9 mm. The intensity distribution was measured at a step interval of 0.05° for a time of 40 s in the range 16.5–18.5° (twice the Bragg angle). To measure the crystal lattice modulus exactly, we took great care to avoid further elongation of the drawn test specimen under the external applied stress at temperatures above 110°C. This is due to the fact that further elongation under a constant stress, termed 'creep', is associated with viscoelastic properties and invalidates the homogeneous stress hypothesis[12].

RESULTS AND DISCUSSION

Figure 1 shows the viscosity measured in distilled water by an Ubbelohde-type capillary viscometer for three kinds of HPC powders of specimens A, B and C. The specific viscosity η_{sp} is defined by $\eta_{sp} = \eta/\eta_0 - 1$, in which η and η_0 are the viscosities of the solution and solvent, respectively. As can be seen in *Figure 1*, η_{sp}/c of specimens A and B shows a gradual increase with concentration. However, that of specimen C shows a remarkably increasing curve, indicating a considerable increase in the number of interpenetrating random coils, which form a large number of coupling entanglements that are both intra- and intermolecular in solution.

Figure 2 shows WAXD and SAXS patterns (end view) of specimen C. The (1 0 0) and (0 1 0) reflections are equivalent, since the unit cell of the HPC crystal is tetragonal. Hence the intense equatorial reflection at $2\theta = 7.8°$ is defined as the (1 0 0) reflection as reported by Samuels[1]. The equatorial reflection at $2\theta = 20.3°$ corresponds to the amorphous halo. The WAXD pattern indicates the slight preferential orientation of the crystal chain axes and amorphous chain segments parallel to the film surface. The SAXS pattern shows no scattering maximum. This indicates that the crystal lamellae are too small to detect by SAXS measurements. Similar profiles of WAXD and SAXS patterns were also observed for specimens A and B.

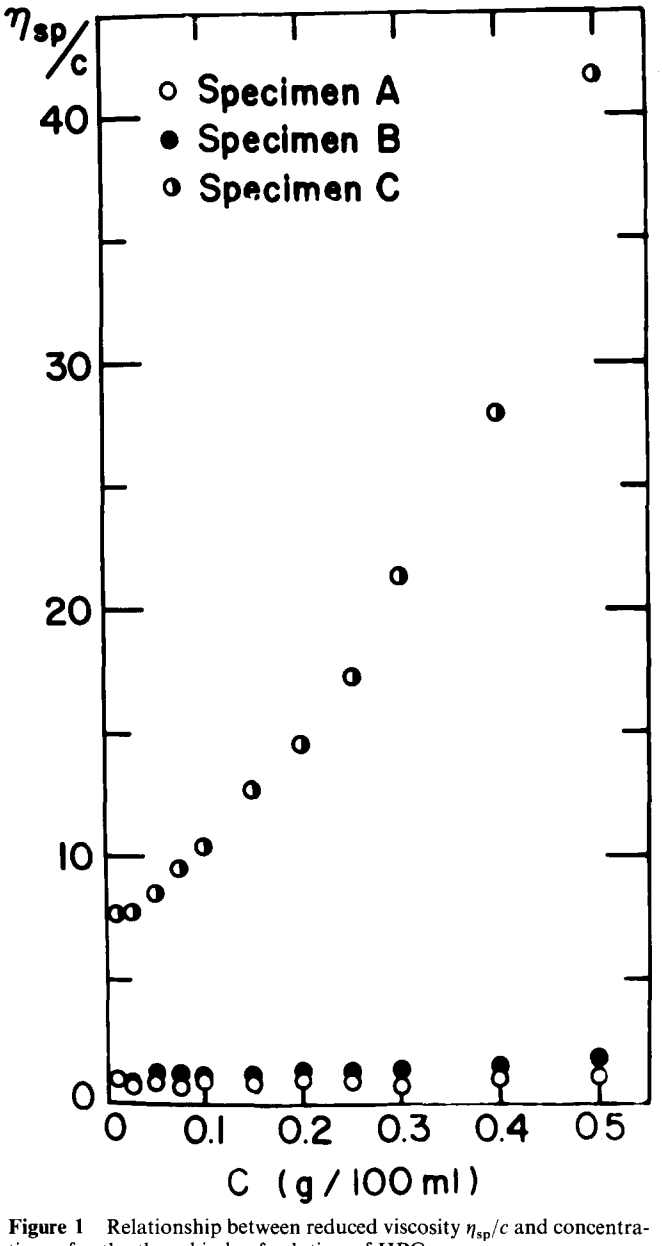

Figure 1 Relationship between reduced viscosity η_{sp}/c and concentration c for the three kinds of solution of HPC

Figure 3 shows the variation of birefringence with draw ratio for the three kinds of specimens. The values increase with increasing λ, and the drawability becomes pronounced with increasing molecular weight. This indicates that molecular chains within specimen A undergo considerable slippage during elongation because of the lack of entanglement meshes, and consequently the specimen breaks at such a low draw ratio as $\lambda = 2.5$. Actually, it is evident that the chain length of HPC within specimen A is much shorter than that of the low-molecular-weight polyethylene (LMWPE) used by Ward[6,7] and Porter[8] to produce high-modulus fibres. Furthermore, it was confirmed that an increase in the crosslink density due to oriented crystallization cannot be expected for the HPC film, as listed in *Table 2*. In *Table 2*, the increase in crystallinity for the HPC films is less pronounced than those of the semicrystalline polymers generally observed. That is, the crystallinity increases slightly from 18.3 to 22.1% with draw ratio. This indicates that bulky poly(propylene oxide) side groups hamper oriented crystallization.

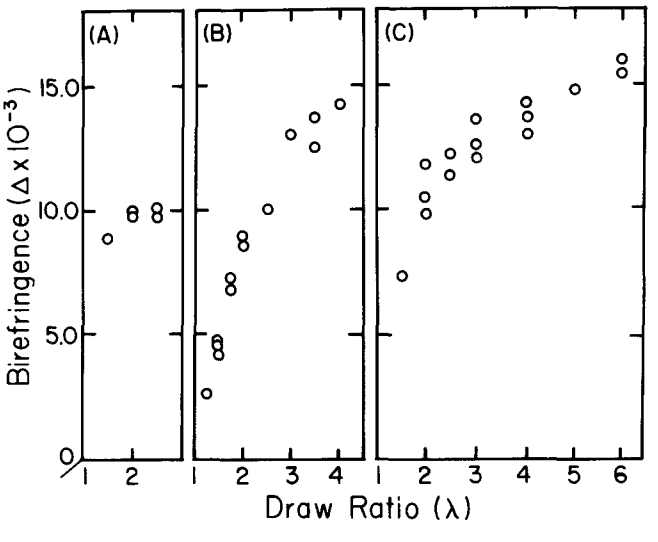

Figure 3 Birefringence of the three kinds of HPC films as a function of draw ratio λ

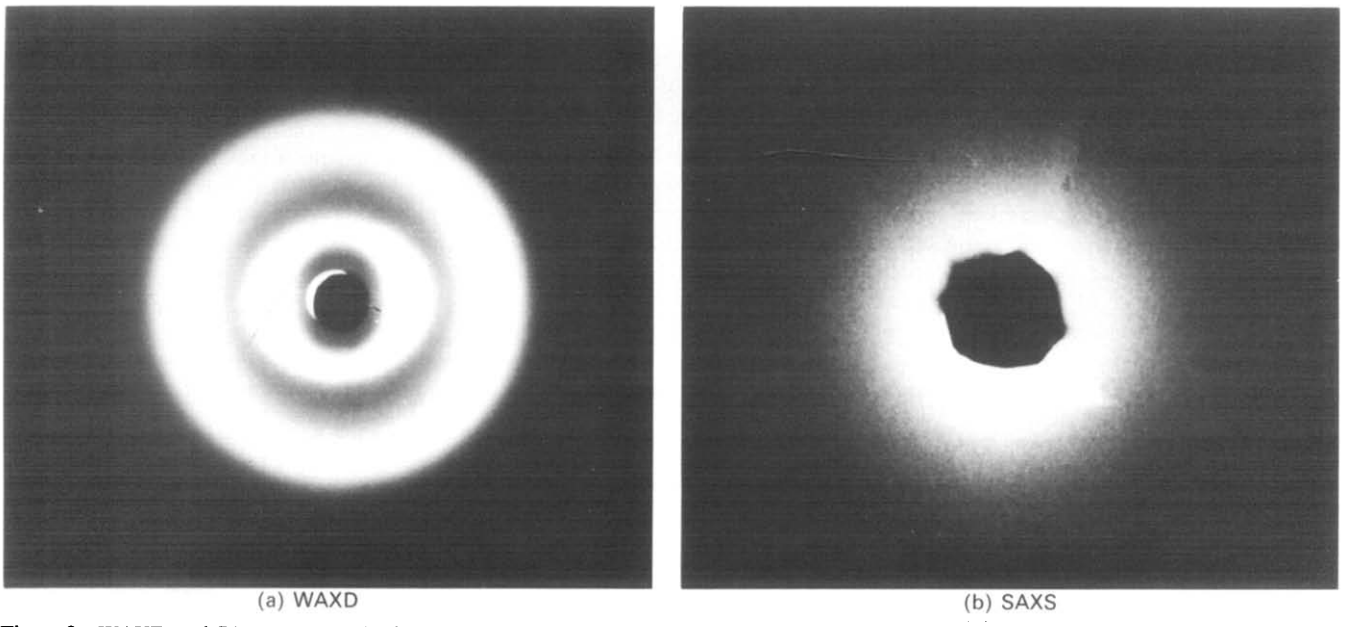

Figure 2 WAXD and SAXS patterns (end view) of specimen C

Table 2 Change in crystallinity of three kinds of HPC films as a function of draw ratio λ

Specimen	Draw ratio	Crystallinity (%)
A	1.0	20.3
	1.2	21.4
	2.0	22.1
	2.5	22.8
B	1.0	20.6
	1.2	21.2
	1.6	21.4
	2.4	21.5
	2.5	21.7
	3.0	21.8
	4.0	22.6
C	1.0	18.3
	2.0	18.9
	3.0	20.8
	4.0	21.2
	5.0	21.5
	6.0	21.7
	7.0	22.1

WAXD patterns (through view) were observed for the three kinds of specimens A, B and C as functions of draw ratio λ. The patterns of specimen C are shown in *Figure 4*. The decreasing angular spread of the strong equatorial (1 0 0) reflection indicates an increase in the degree of orientation of the c axis with respect to the stretching direction.

Figure 5 shows representative values of tensile strength as a function of draw ratio for the three kinds of specimens, based on the nominal stress–elongation curves. The strain speed was selected to be 4 mm min^{-1}. The values were obtained on the basis of several measurements at a given draw ratio. It should be noted that, in determining the stress corresponding to each elongation, the values of the tensile force were divided by the cross-sectional area of the original specimens. Hence, if the tensile force is divided by the cross-sectional area of the specimen at each elongation, the true stress, rather than the nominal stress, is obtained. The increase in true stress with draw ratio λ is, of course, more marked. The maximum value for specimen C reached 0.14 GPa at $\lambda = 6.0$. Here it should be noted that the tensile strength at each draw ratio less than 4 becomes more pronounced as the molecular weight decreases, although the birefringence at each draw ratio is almost independent of the molecular weight. This phenomenon is probably due to the fact that the strains of tie molecules and/or entanglements within the specimen are more intense as the molecular weight decreases. Further elongation beyond $\lambda = 2.5$ was impossible for specimen A because of considerable slippage between polymer chains, leading to the disappearance of crosslinking points.

Figure 6 shows the temperature dependence of the real and imaginary parts of the complex dynamic tensile modulus of the drawn specimens. The magnitude of the storage modulus E' decreases as the temperature increases. The value of E' of specimen C with $\lambda = 6$ was about 7 GPa at 20°C. Draw ratio causes significant change in the profile of the temperature dependence of loss modulus E''. The curve of E'' as a function of temperature exhibits two peaks. One peak appeared around 0°C and the other in the range from 70 to 100°C. This phenomenon is independent of draw ratio ($\lambda = 2.5$–6) and molecular weight. The former peak is probably associated with the transition from the glassy to the rubber-like state due to segmental motions in the amorphous phase. The latter peak is probably attributed to the active mobility of water molecules, which play an important role as a plasticizer by disruption of interchain hydrogen bonds. Actually, this behaviour invokes rubber elasticity and allows the gradual decrease in the storage modulus in the temperature range 40–60°C.

Figure 7 shows the crystal lattice modulus at room temperature and *Figure 8* shows the temperature dependence of the crystal lattice modulus. Judging from both figures, the crystal lattice modulus is independent of temperature below 150°C, and it decreases considerably at 170°C. Such a temperature dependence of the crystal lattice modulus is quite different from the storage (or Young's) modulus as shown in *Figure 6*. Such behaviour has been observed for ultradrawn polyethylene and polypropylene films[12,13]. Here it should be noted that, if the HPC unit cell reported by Samuels is employed[1], the cross-section of the unit cell perpendicular to the chain direction is about 128 $Å^2$. This value is about twice the corresponding cross-sections of the crystal unit cells of cellulose I and II[14,15]. However, the value of the crystal lattice modulus is about one-fifth of that of cellulose I and one-quarter of that of cellulose II[16]. This is probably due to unstable packing of HPC molecules within the crystal unit because of the existence of bulky poly(propylene oxide) side groups.

In order to study the different temperature dependences of the crystal lattice modulus and the storage modulus, the thermal properties in bulk were studied by d.s.c. and X-ray diffraction. *Figure 9* presents d.s.c. data, in which the curves correspond to specimens with $\lambda = 1$, 5 and 7, respectively. For these curves, there are no endotherm and exotherm peaks. This phenomenon is quite different from the result reported by Samuels[1]. According to his report, the major melting peak appeared at 208°C, while the temperature at which the last crystal melts was 234°C. The d.s.c. curves indicating no melting point in *Figure 9* are insufficient to explain the decrease in the storage modulus with temperature in *Figure 6*, and therefore the temperature dependence of crystallinity was observed for specimen C with $\lambda = 7$.

In order to estimate the above phenomenon quantitatively, the total diffraction intensities from the (1 0 0) and (0 0 2) planes in the meridional and vertical directions were observed as a function of temperature T. The intensity $I(T, S)$ was measured at a step interval of 0.1° for a time of 10 s in the angle range 4–27° (twice the Bragg angle 2θ) for (1 0 0) plane and in the angle range 15–20° for the (0 0 2) plane with a fixed dimension in the stretching direction. The estimation was represented as a function of IS^2 *versus* S ($S = 2 \sin \theta/\lambda$, λ being the X-ray wavelength)[17]. All intensities at the indicated temperatures were normalized by that at 20°C, which is given by:

$$\text{Normalized value} = \frac{\int_{S_1}^{S_2} I(T, S)S^2 \, dS}{\int_{S_1}^{S_2} I(T = 20°, S)S^2 \, dS} \quad (1)$$

where S_1 and S_2 correspond to S ($= 2 \sin \theta/\lambda$) at $\theta_1 = 2.7°$ and $\theta_2 = 7.0°$, respectively, for the (1 0 0) plane, and at

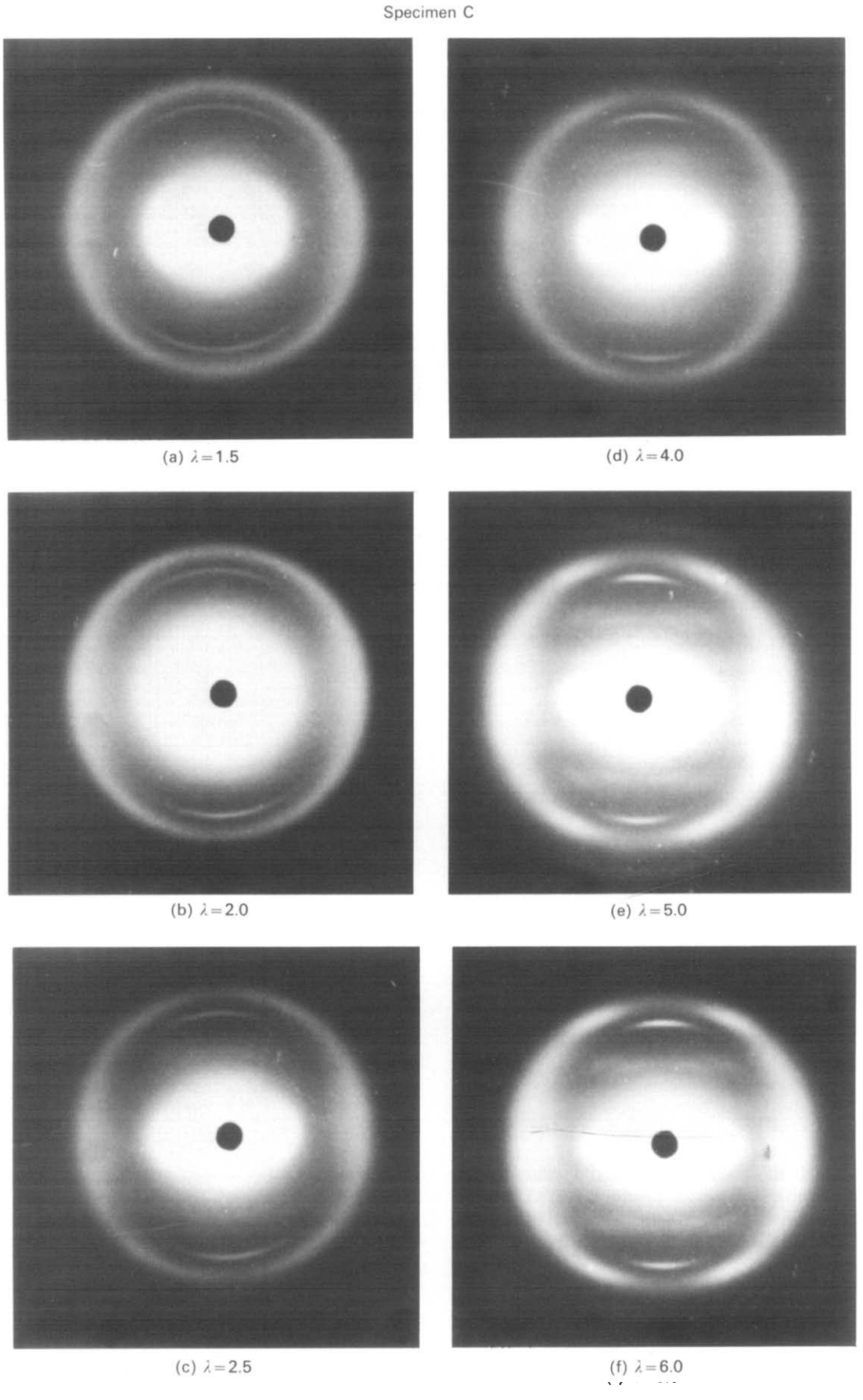

Figure 4 WAXD patterns (through view) of specimen C with draw ratio λ

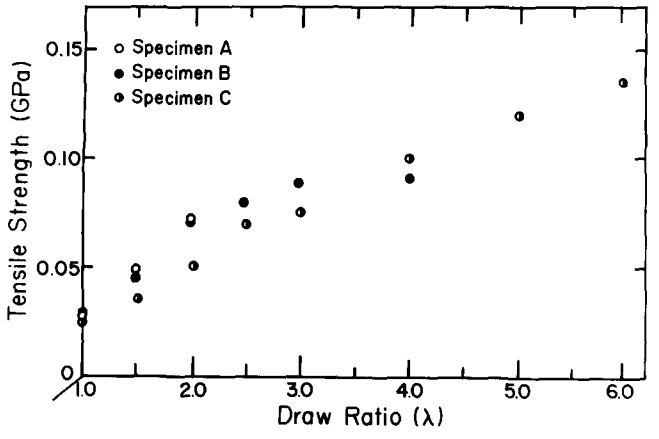

Figure 5 Tensile strength of the three kinds of HPC films as a function of draw ratio λ

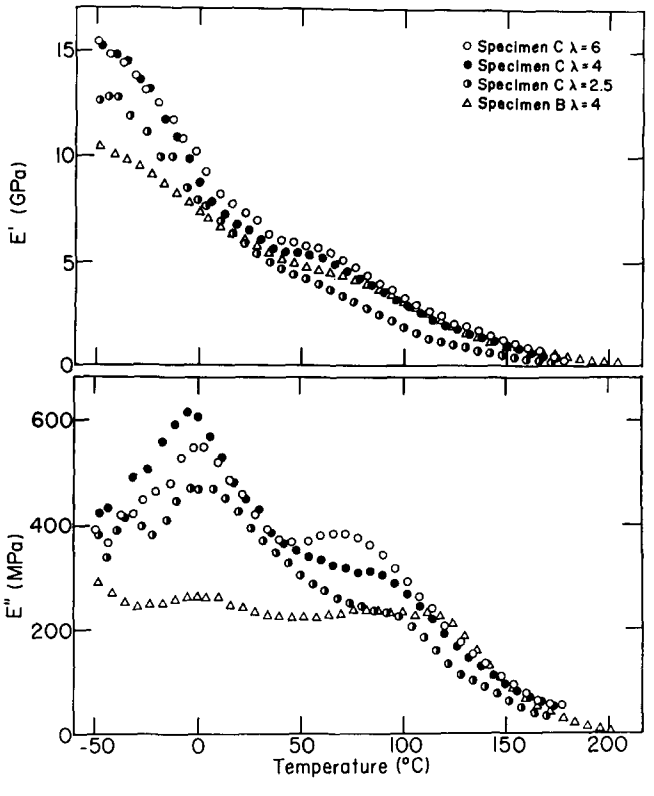

Figure 6 Temperature dependence of the storage and loss moduli of the indicated specimens

$\theta_1 = 7.65°$ and $\theta_2 = 9.60°$, respectively, for the (0 0 2) plane.

Figure 10 shows the results for the (0 0 2) and (1 0 0) planes. Both values show a gradual increase with temperature. Conversely, each value for the (0 0 2) and (1 0 0) planes becomes smaller beyond 130 and 170°C, respectively. This means that the growth of crystallites becomes more pronounced with increasing temperature up to 130°C. With further increasing temperature beyond 130°C, the growth of crystallites in the chain direction becomes less pronounced because of an increase in thermal fluctuation arising from lattice distortion. In contrast, the further growth of crystallites in the direction perpendicular to the chain axis was observed up to 170°C, indicating a slight increase in thermal crystallization. Finally, at 180°C, the sample was broken because of main-chain scission due to thermal decomposition.

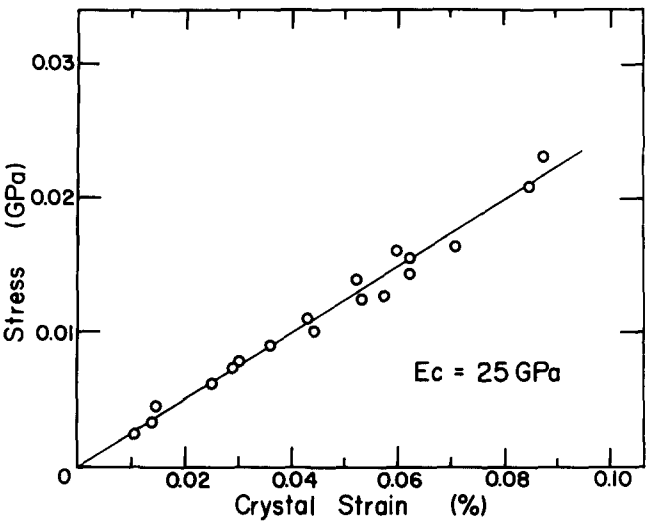

Figure 7 Crystal lattice modulus of HPC at room temperature

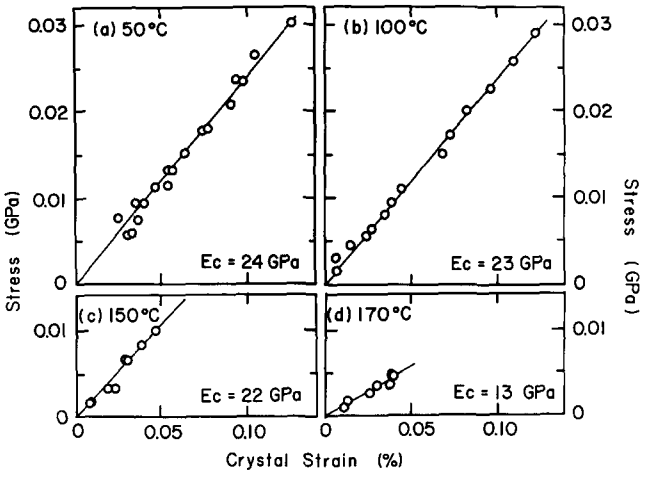

Figure 8 Temperature dependence of crystal lattice modulus of HPC

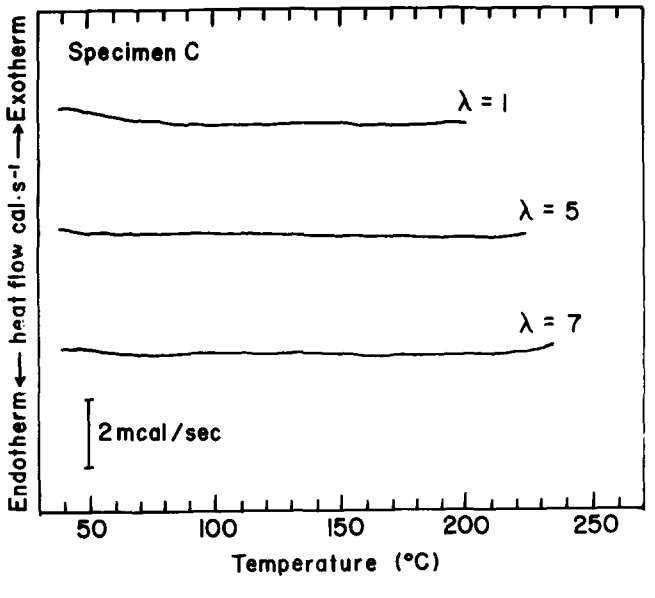

Figure 9 D.s.c. curves of specimen C measured for various draw ratios λ

Anyway, it may be noted that the crystallinity increases with temperature up to 130°C. This tendency is quite different from the results obtained for ultradrawn polyethylene[12] and polypropylene films[13]. According to the previous work[12,13], it was concluded that the decrease in their Young's (storage) moduli with temperature is attributed to the decrease in their crystallinities. However, the decrease in the Young's (storage) modulus of HPC having no distinct melting point cannot be explained on the basis of the above concept. To solve this question, the average distance between the amorphous chain segments is estimated by using the Bragg equation. The intensity distribution function of the amorphous halo was obtained by subtracting background noise and air scattering from total intensity, and the peak position was assumed to be equal to the centre of gravity of the intensity distribution function of $2\theta_B$ in the horizontal direction by setting θ_1 and θ_2 to 7.1° and 12.5°, respectively. This treatment was done because of the difficulty in determining the peak position of the broad distribution function associated with the contribution of the intensity from the amorphous phase. The procedure to obtain the centre of gravity was described in detail elsewhere[11]. The results are shown in *Table 3*. The average distance becomes longer with increasing temperature, indicating active mobility of amorphous chain segments. Therefore, it may be concluded that the decrease in the Young's (storage) modulus of HPC is due to thermal expansion of the average distance between the amorphous chain segments, and this phenomenon is quite different from the behaviour of polyethylene and polypropylene films with a distinct melting point[12,13].

Figures 11 and *12* show the Hv patterns obtained in the process of evaporation of solvent from a solution of specimen B with concentration 10 g/100 ml and a solution of specimen C with concentration 5 g/100 ml, respectively. The indicated time (min) was defined after the first pattern (0 min) appeared. The photographs of specimen B show +-type patterns at small angles and ×-type patterns with a scattering maximum at large angles. Such profiles were observed by Hashimoto *et al.*[18]. The intensity of the small-angle scattering increases with time, i.e. with increasing concentration, and becomes stronger than that of the wide-angle scattering. The wide-angle scattering maximum shifts only slightly towards smaller angle and, finally, the patterns evolve into a typical +-type pattern. The intensity minimum at odd multiples of $\mu = 45°$ is a consequence of superposition of the two types of scattering patterns. The same phenomenon was also observed for specimen A. In contrast, the photographs of specimen C show a +-type pattern, indicating scattering from rods with random orientations. The pattern becomes clearer and the intensity increases with time, i.e. with increasing concentration. The ×-type pattern could not be observed in any stage. This indicates that the formation of superstructures by the evaporation of solvent is dependent upon the molecular weight of the test specimen.

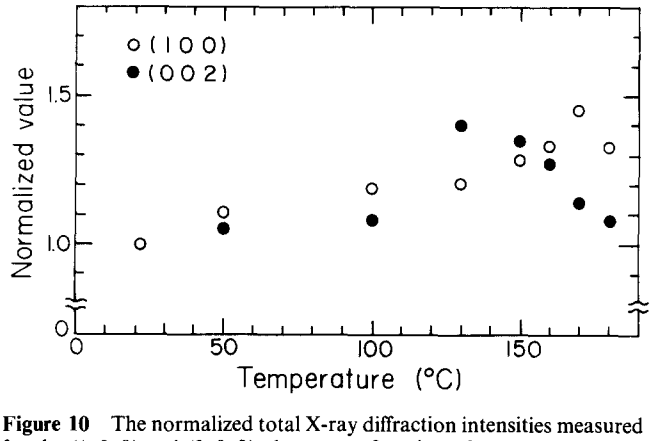

Figure 10 The normalized total X-ray diffraction intensities measured for the (1 0 0) and (0 0 2) planes as a function of temperature

As concluded for scattering from an assembly of rods, we believe that the ×-type patterns at large angles shown in *Figures 11a* and *11b* reflect interparticle interference effects from the rods in the solution, but this effect becomes ambiguous with increasing concentration. This behaviour can be analysed in terms of an increase in orientational fluctuation of rods and a decrease in medium between rods due to to an increase in rod width leading to evaporation of solvent. In these figures, the +-type patterns for all undrawn films showed a four-fold symmetrical intensity distribution with maximum intensities at azimuthal angle 0° (meridian) and 90° (equator) and the intensity decreased continuously with increasing scattering angle. Consequently, the patterns are indicative of typical scattering from anisotropic rods, the optical axes being oriented at 45° with respect to the rod axis[19].

Figures 13–15 show changes of Hv scattering patterns upon stretching of the respective three kinds of film. At the initial elongation ratio, the meridional lobes of the pattern become diffuse and thick, while the equatorial lobes become sharply extended. This mechanism cannot be explained in terms of a simple affine deformation model concerning an isolated rod[1,18].

A drastic change of the pattern for each specimen, however, arises at $\lambda = 1.5$ for specimen A, at $\lambda = 1.5$ for specimen B, and at $\lambda = 2.0$ for specimen C. Some ×-type scattering lobes appear in addition to sharp streaks in the equatorial directions, and the lobes are extended in the horizontal direction with increasing λ. The drastic changes of the scattering patterns are attributed to the effect of scattering from assemblies of rods. Namely, we believe that the streaks reflect interparticle interference effects from the rods. It may be expected that the assembly of rods is maintained within the resultant cast film, in spite of the disappearance of the ×-type pattern at small angles in the process of evaporation of solvent.

Table 3 Temperature dependence of the average distance between amorphous chain segments, estimated by the Bragg equation

	Temperature (°C)							
	22	50	100	130	150	160	170	180
Average distance (Å)	4.71	4.72	4.74	4.75	4.76	4.77	4.79	4.80

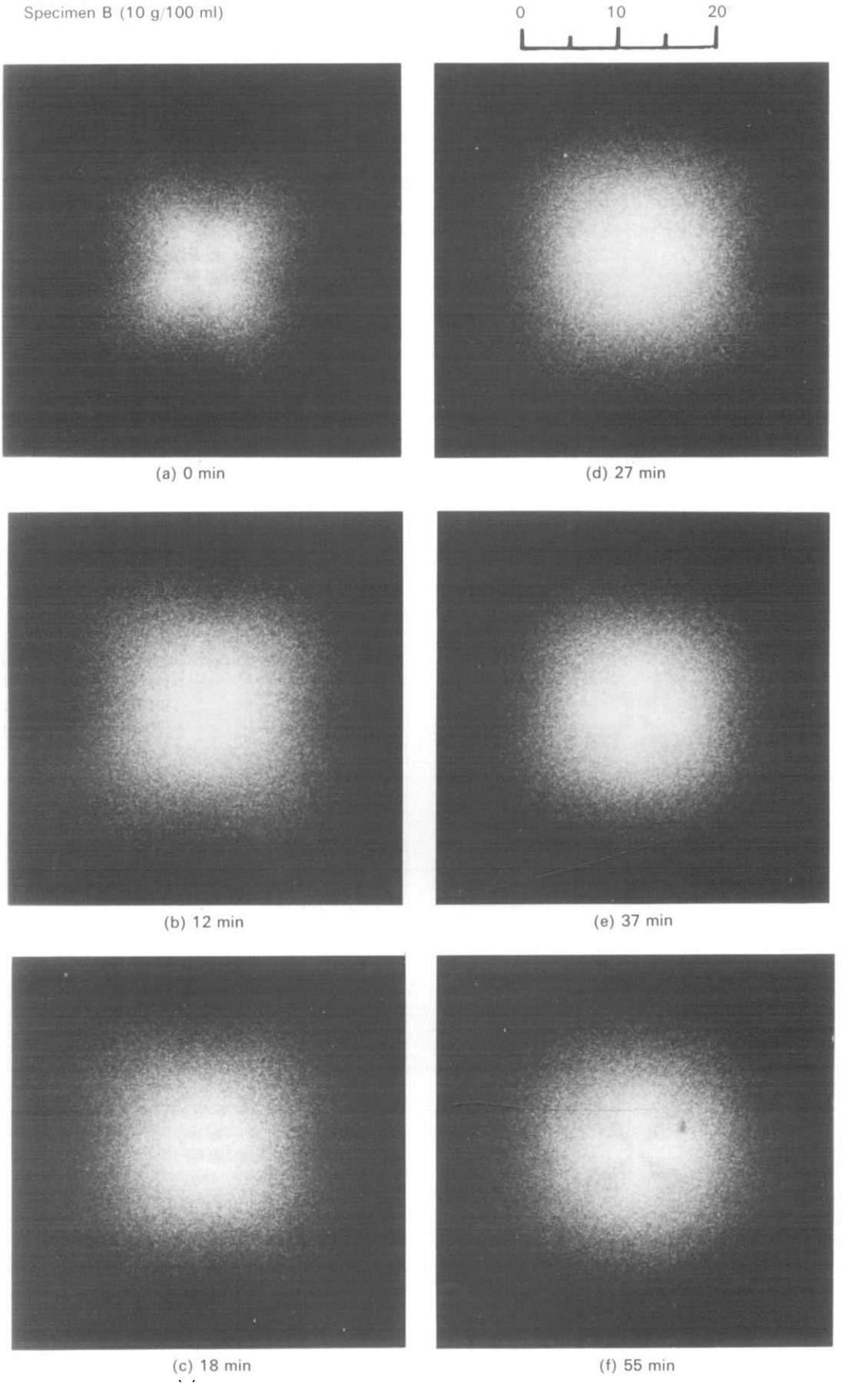

Figure 11 Hv patterns obtained during evaporation of solvent from a solution of specimen B

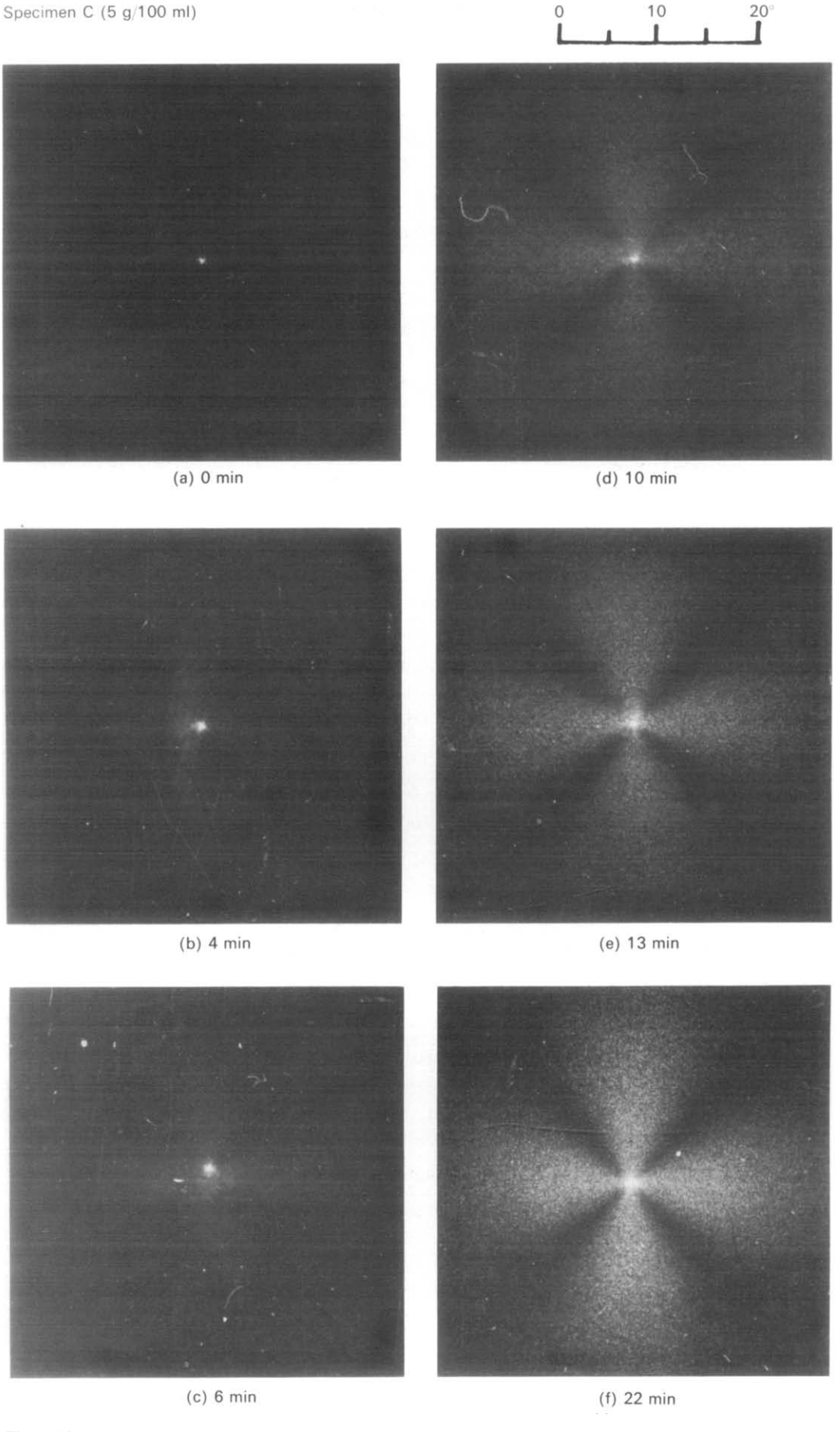

Figure 12 Hv patterns obtained during evaporation of solvent from a solution of specimen C

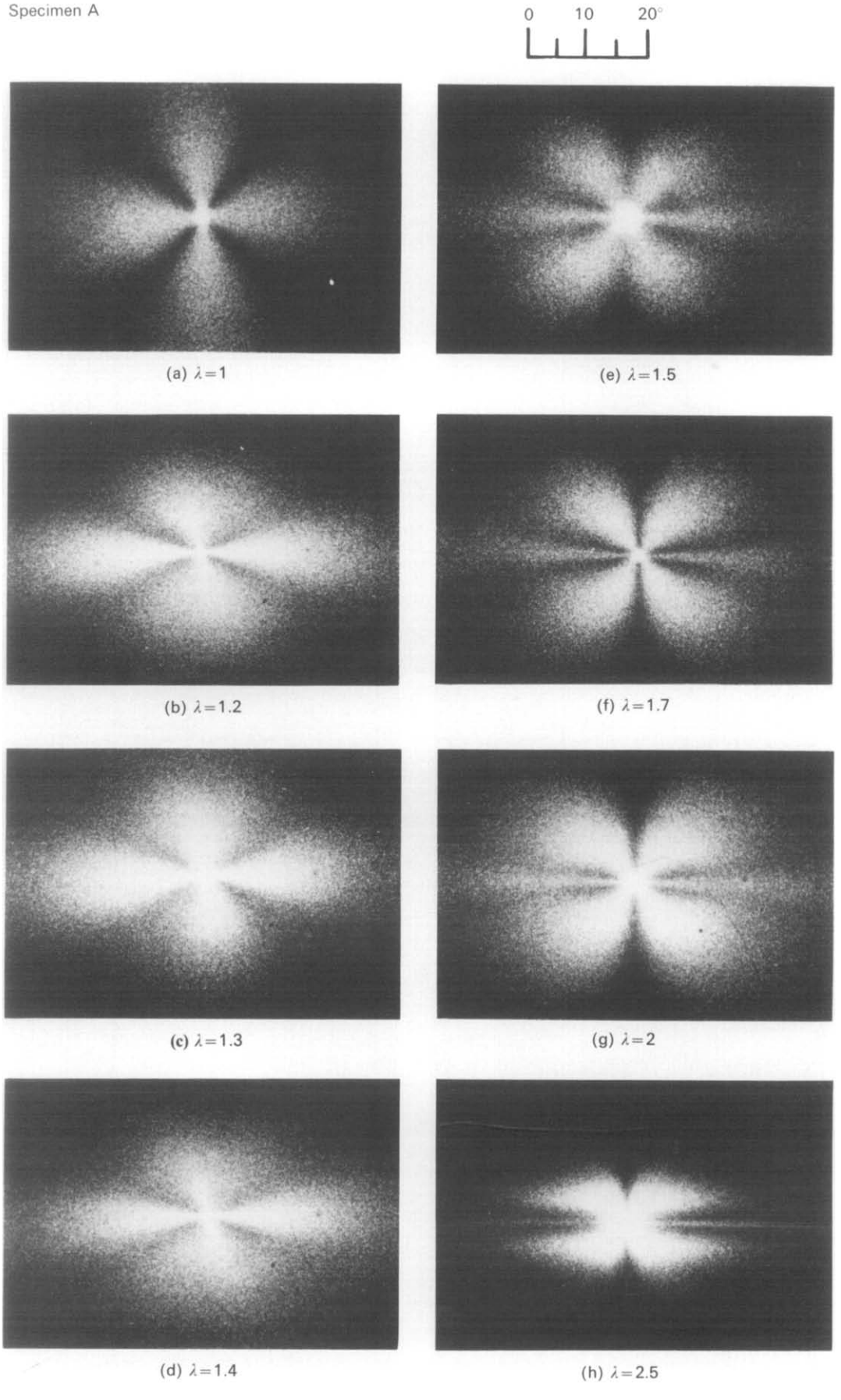

Figure 13 Change in Hv patterns from specimen A at various draw ratios λ

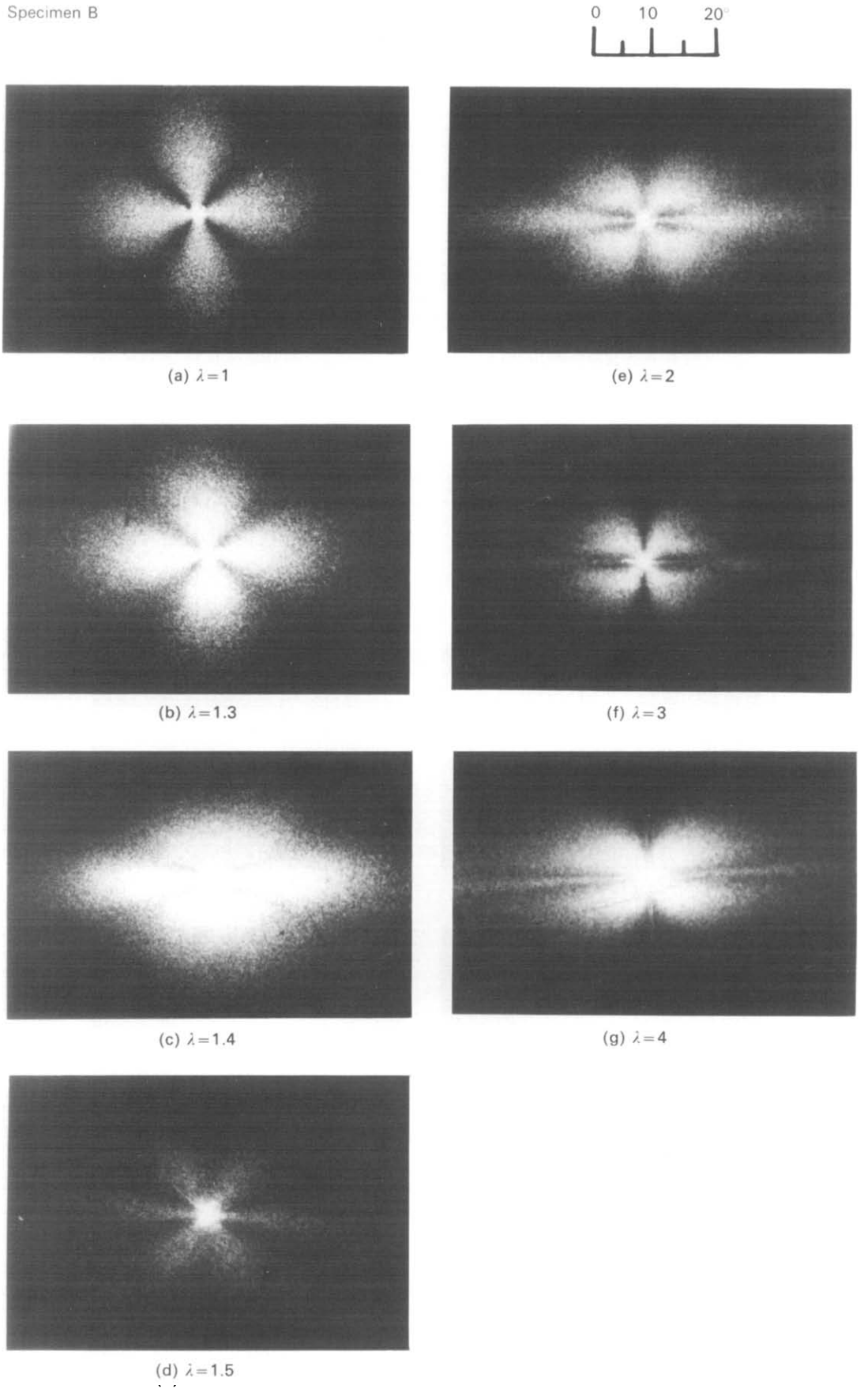

Figure 14 Change in Hv patterns from specimen B at various draw ratios λ

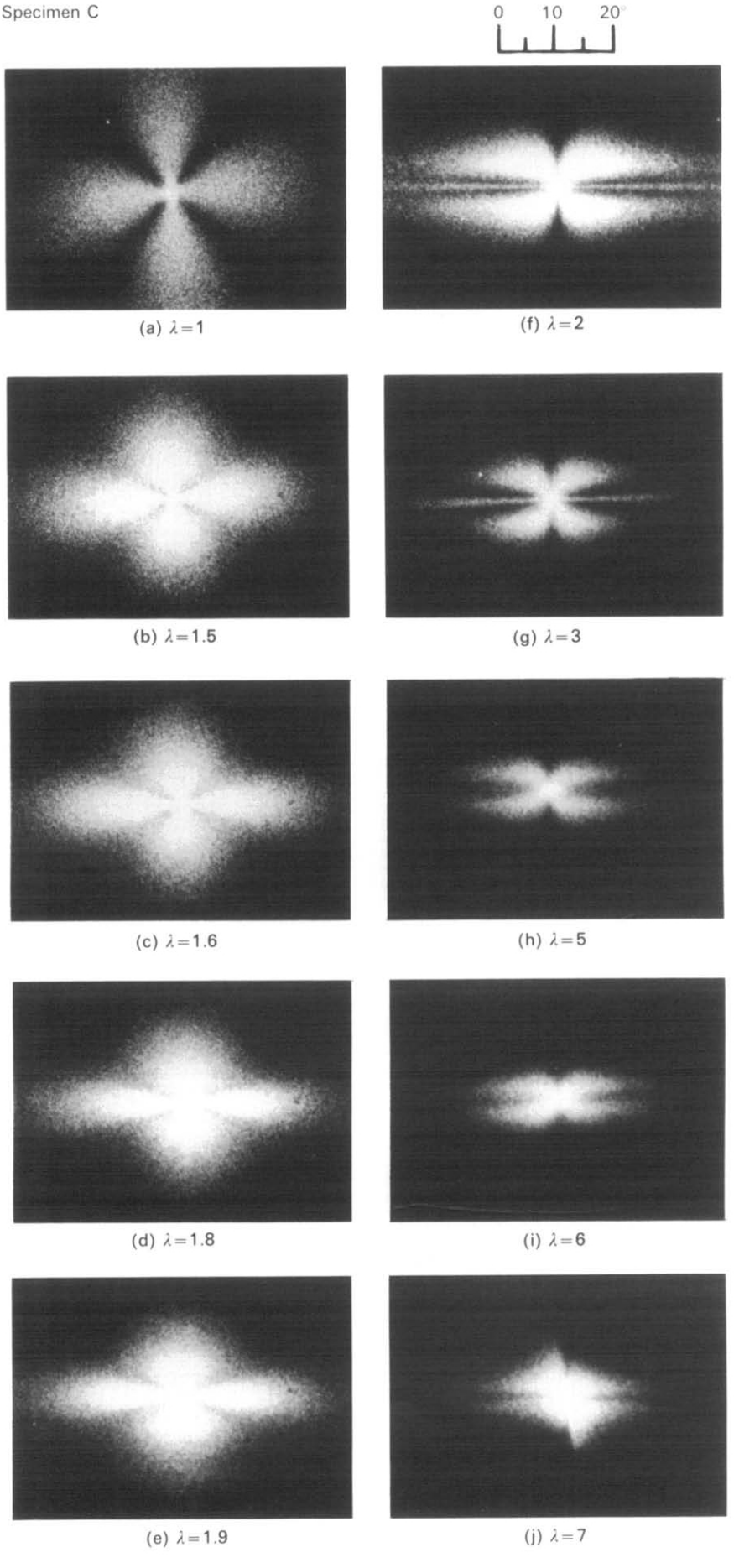

Figure 15 Change in Hv patterns from specimen C at various draw ratios λ

Elongation of the resultant film beyond $\lambda = 1.5$ causes further development of the ordered orientation of the rods, enough to reflect the interparticle interference effects in the scattering patterns of specimens A and B. As mentioned before, the drastic change of the scattering pattern from +-type to ×-type shifts to higher draw ratio with molecular weight as shown in *Figures 13–15*. This phenomenon is thought to be due to the molecular-weight dependence of the assembly mode of rods within undrawn films ($\lambda = 1$). From the patterns shown in *Figures 11* and *12*, it may be expected that the degree of ordered arrangement of rods within specimens A and B, showing ×-type patterns in the process of evaporation of solvent, is more significant than that of specimen C. To give more conclusive evidence, theoretical analysis of a series of scattering patterns must be carried out.

The analysis of the scattering patterns from drawn HPC films has been carried out by Samuels[1] and Hayashi *et al.*[20] on the basis of scattering from an oriented rod. These patterns calculated on this basis were in good agreement with the patterns observed at initial elongation ratios up to $\lambda = 1.5$ for specimens A and B and up to $\lambda = 2.0$ for specimen C. The appearance of the sharp streaks, however, could not be explained. Therefore, a new calculation method must be proposed to consider interparticle interference effects.

Figure 16 shows a model system to calculate light scattering patterns theoretically. Efforts have been made to preserve the notation of Blundell[21] in order to emphasize the similarity of formulation between small-angle light scattering and small-angle X-ray scattering. In this model system, vector $\boldsymbol{k}$ corresponds to the stretching direction and vector $\boldsymbol{j}$ is parallel to the direction of the incident beam, whose unit vector is defined as $\boldsymbol{S}_0$. The intensity distribution is observed as a function of scattering angle θ and the azimuthal angle μ, and $\boldsymbol{S}'$ is a unit vector along the scattered laser beam.

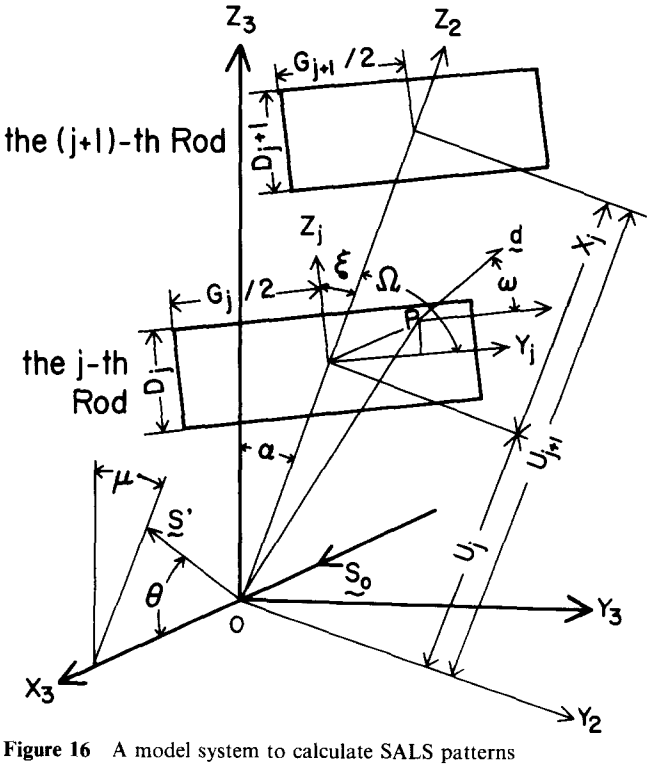

Figure 16 A model system to calculate SALS patterns

Judging from the WAXD pattern (end view) in *Figure 2*, we believe that the rods are oriented on the two-dimensional plane. Hence the rods are assumed to be rectangular in cross section and to be situated in the plane OY_3Z_3. The centre of gravity of each rod is in the direction of the Z_3 axis. As for the jth rod, the Y_j and Z_j axes are parallel and perpendicular, respectively, to the direction of the rod axis and Ω denotes the orientational angle between Y_j and Z_2 axes. The dimensions of the jth rod are represented by the length L_j and the width D_j and α denotes the orientational angle between Z_3 and Z_2 axes. The optical axis is assumed to be oriented at polar angle ω with respect to the rod axis and to lie in a rectangular plane.

Considering the geometrical arrangement of the rods in *Figure 16*, the normalized scattered intensity from an assembly of N rods can be obtained by the method proposed by Blundell[21]. As a result:

$$I = I_B - I_C \tag{2}$$

where I_B and I_C are given by:

$$I_B = \mathrm{Re}\left(J - G_y^2 + \frac{1+F_x}{1-F_x} G_y^2\right) \tag{3}$$

and

$$I_C = \mathrm{Re}\left(\frac{2G_y^2 F_x(1-F_x^N)}{N(1-F_x)^2}\right) \tag{4}$$

Here

$$J = \int_0^{2\pi}\int_{-\infty}^{\infty}\int_{-\infty}^{\infty} P(\alpha)H(D_j)M(G_j)f_j^2 \mathrm{d}D_j\,\mathrm{d}G_j\,\mathrm{d}\alpha \tag{5}$$

$$G_y = \int_0^{2\pi}\int_{-\infty}^{\infty}\int_{-\infty}^{\infty} P(\alpha)H(D_j)M(G_j)f_j^2\,\mathrm{d}D_j\,\mathrm{d}G_j\,\mathrm{d}\alpha \tag{6}$$

$$F_x = \int_{-\infty}^{\infty} h(X_j)\exp(-2\pi i b X_j)\,\mathrm{d}X_j \tag{7}$$

and

$$b = \sin\theta\cos\mu/\lambda' \tag{8}$$

where λ' is the wavelength in the medium and f_j is the scattering amplitude from the jth rod.

Following Blundell[21], we assume that the variations of the lengths L_j, D_j and X_j are independent of each other and are given by the following symmetrical functions with respective mean lengths $\bar{L}$, $\bar{D}$ and $\bar{X}$ and standard deviations σ_D, σ_G and σ_X:

$$H(D_j) = \frac{1}{\sqrt{2\pi}\,\sigma_D}\exp\left(-\frac{(D_j-\bar{D})^2}{2\sigma_D^2}\right) \tag{9}$$

$$M(G_j) = \frac{1}{\sqrt{2\pi}\,\sigma_G}\exp\left(-\frac{(G_j-\bar{G})^2}{2\sigma_G^2}\right) \tag{10}$$

and

$$h(X_j) = \frac{1}{\sqrt{2\pi}\,\sigma_X}\exp\left(-\frac{(X_j-\bar{X})^2}{2\sigma_X^2}\right) \tag{11}$$

Assuming the affine deformation of the rods, the scattering amplitude f_j from the jth rod may be given by:

$$f_j = \cos\rho\left(\frac{\lambda_2\lambda_3\cos(\alpha+\Omega-\omega)\sin(\alpha+\Omega-\omega)}{\lambda_2^2\sin^2(\alpha+\Omega-\omega)+\lambda_3^2\cos^2(\alpha+\Omega-\omega)}\right) \times \frac{\sin[A_j(\alpha)]}{A_j(\alpha)}\frac{\sin[B_j(\alpha)]}{B_j(\alpha)} \tag{12}$$

Here

$$A_j(\alpha)=\frac{1}{2}W[\lambda_2\sin\mu\sin(\alpha+\Omega)+\lambda_3\cos\mu\sin(\alpha+\Omega)] \quad (13)$$

$$B_j(\alpha)=\frac{1}{2}W(\bar{D}/\bar{G})[\lambda_2\sin\mu\sin(\alpha+\Omega)+\lambda_3\cos\mu\sin(\alpha+\Omega)] \quad (14)$$

$$\cos\rho=\cos\theta/(\cos^2\theta+\sin^2\theta\sin^2\mu)^{1/2} \quad (15)$$

and

$$W=2\pi(\bar{G}/\lambda)\sin\theta \quad (16)$$

where λ_3 and λ_2 are draw ratios imposed on the rod along and perpendicular to the stretching direction.

Furthermore, J, G and F_x may be represented concretely as follows:

$$J=\cos^2\sigma_2\int_0^{2\pi}C^2(\alpha)\times\{1-\cos[2A_j(\alpha)]\exp[-2(\sigma_G/\bar{G})^2A_j^2(\alpha)]\}/2A_j^2(\alpha)\times\{1-\cos[2B_j(\alpha)]\exp[-2(\sigma_D/\bar{D})^2B_j^2(\alpha)]\}/2B_j^2(\alpha)\,d\alpha \quad (17)$$

$$G_y=\cos\rho\int_0^{2\pi}C(\alpha)\times\{\sin[A_j(\alpha)]/A_j(\alpha)\}\exp\left[-\frac{1}{2}(\sigma_G/\bar{G})^2A_j^2(\alpha)\right]\times\{\sin[B_j(\alpha)]/B_j(\alpha)\}\exp\left[-\frac{1}{2}(\sigma_D/\bar{D})^2B_j^2(\alpha)\right]d\alpha \quad (18)$$

and

$$F_x=\exp[-W^2/2(\sigma_G/\bar{G})^2(\lambda_3\cos\mu\cos\alpha+\lambda_2\sin\mu\sin\alpha)^2]\times\exp[(\bar{X}/\bar{G})W(\lambda_3\cos\mu\cos\alpha+\lambda_2\sin\mu\sin\alpha)] \quad (19)$$

where

$$C(\alpha)=\frac{\lambda_2\lambda_3\cos(\alpha+\omega)\sin(\alpha+\omega)}{\lambda_2^2\sin^2(\alpha+\omega)+\lambda_3^2\cos^2(\alpha+\omega)} \quad (20)$$

In a real system, the position of the specimen sampled by the laser beam contains a distribution of the number of rods N. This concept cannot be introduced in order to smear out the many subsidiary maxima that appear at smaller scattering angle. This has been taken into consideration by Hashimoto *et al.*[20], who introduced a discrete symmetrical distribution of N with standard deviation $\sigma_N=3$ in order to calculate small-angle X-ray and light scattering intensities. This distribution is written as:

$$P(N)=\frac{\exp[-(N-\bar{N})^2/2\sigma_N^2]}{\sum_{N=1}^{2\bar{N}-1}\exp[-(N-\bar{N})^2/2\sigma_N^2]} \quad (21)$$

In the present work, we will assume the same type of distribution of N. Then, the average value of the term I_C is given by:

$$\langle I_C\rangle_{av}=\sum_{N=1}^{2\bar{N}-1}I_CP(N) \quad (22)$$

In our subsequent calculations, we assume an average $\bar{N}$ of 10.

According to the theoretical analysis, the scattered intensity depends upon the structural parameters $\sigma_G/\bar{G}$, $\sigma_D/\bar{D}$, $\sigma_X/\bar{X}$, $\bar{D}/\bar{G}$ and $\bar{G}/\bar{X}$. Before carrying out the numerical calculations of the scattered intensity, the intensity in equation (2) is normalized by $(\bar{D}\,\bar{G})^2$ on the numerical calculation, since the area of each rod is related to the absolute intensity but not to the profile of the intensity distribution function.

Let us consider the μ dependence of the scattered intensity distribution. *Figure 17* shows the patterns calculated for Ω and ω in an undeformed state, in which the values of p $(=\bar{D}/\bar{G})$, q $(=\bar{G}/\bar{X})$, $\sigma_X/\bar{X}$, $\sigma_G/\bar{G}$ and $\sigma_D/\bar{D}$ are fixed. That is, the parameters describing the degrees of fluctuation in the rod length and width are set at very small values such as $\sigma_G/\bar{G}=\sigma_D/\bar{D}=0.01$ and the parameter describing the fluctuation in the long period is fixed at $\sigma_X/\bar{X}=0.5$, to simplify the analysis for the calculated patterns[22]. Furthermore, $\lambda_2\lambda_3=1$ is assumed, to assure linear deformation. The values p and q must be selected to avoid overlapping of neighbouring rods.

As illustrated in *Figure 17*, the patterns at $\omega=0$ (or 90°) and $\Omega=45°$ show +-type lobes at smaller scattering angle and ×-type at wider scattering angle. The appearance of ×-type lobes at wider angles is due to the fact that the optical axes are parallel or perpendicular to the axis of the rod assembly. The scattering lobes showing +-type at smaller angles are due to the orientation of the optical axes at $=45°$ with respect to the Z_2 axis.

Comparing the four patterns, the product of parameters p and q causes a significant effect on the patterns. The profile of +-type becomes sharper with increasing pq $(=\bar{D}/\bar{X})$. In contrast, the profile of ×-type at wider scattering angle becomes duller and the intensity becomes weaker with increasing pq. Comparing these four calculated patterns with the observed ones in *Figures 11a* and *11b*, the pattern (d) calculated at $\bar{D}/\bar{X}=0.8$ is

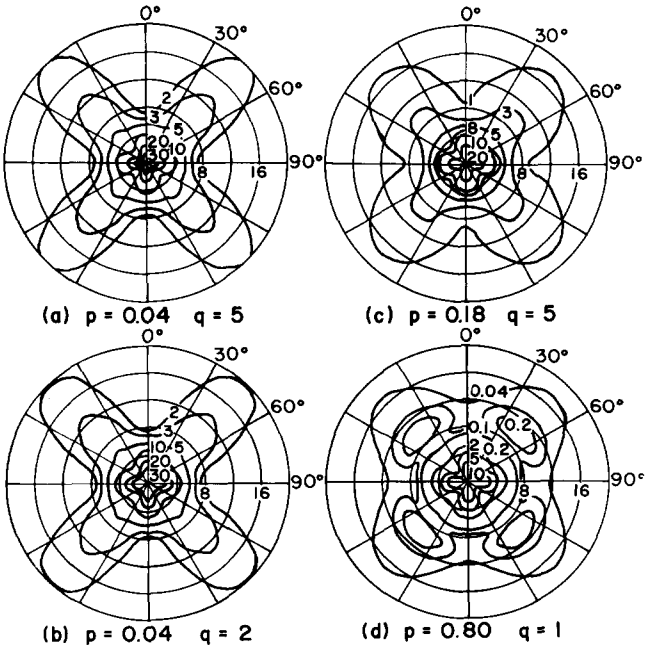

Figure 17 Hv light scattering patterns from an undrawn film with changes in p and q, in which the other parameters are fixed at $\sigma_G/\bar{G}=\sigma_D/\bar{D}=0.01$, $\sigma_X/\bar{X}=0.5$ and $G/\lambda'=20$

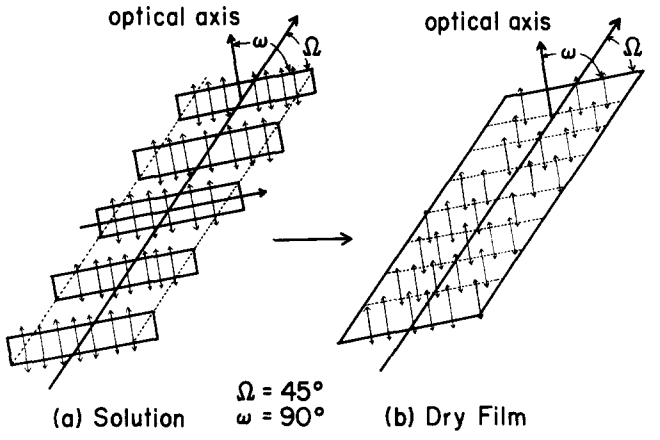

Figure 18 A model representing the formation of rods under evaporation of solvent

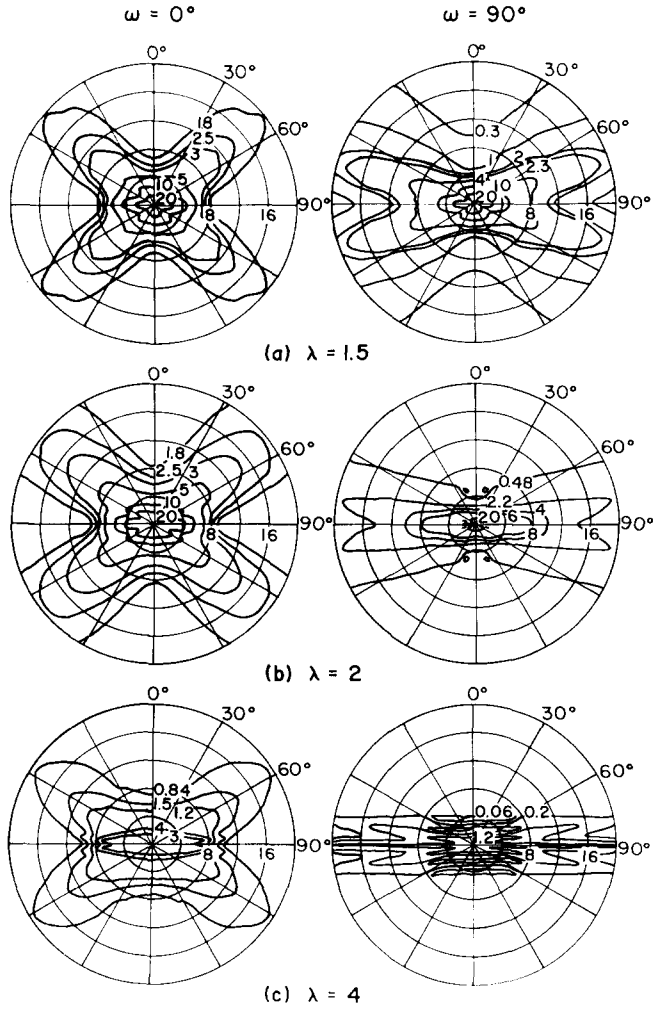

Figure 19 Hv light scattering patterns as a function of draw ratio, in which parameters are fixed at $p = 0.04$, $q = 5$, $\sigma_G/\bar{G} = \sigma_D/\bar{D} = 0.01$, $\sigma_X/\bar{X} = 0.5$ and $\bar{G}/\lambda = 40$

similar to the one observed. This indicates that the distance between rods, $\bar{X}$, is only a little bit longer than the average rod width $\bar{D}$. Therefore, the disappearance of the ×-type pattern can be justified, if the width of rods increases or the gap between rods corresponding to $(\bar{X} - \bar{D})$ becomes close to zero through the evaporation of solvent. Thus, one model is proposed in *Figure 18* to represent the above process. However, if this is the case, the observed +-type pattern must be much smaller on increasing the concentration of solution. This remains an unresolved problem.

Figures 19 and *20* show the scattering patterns as a function of draw ratio λ, in which the patterns on the left- and right-hand sides were calculated at $\omega = 0$ and 90°, respectively. The calculations of patterns in *Figures 19* and *20* were carried out using the corresponding values of p and q in the patterns in *Figures 17b* and *17d*. In the patterns in *Figure 19*, inner +-type lobes are extended in the horizontal direction and ×-type lobes at wider angles are also extended in the horizontal one. The profiles of these +-type lobes, however, are different from those with sharp and long streaks in the horizontal direction observed in *Figures 13–15*. The patterns in *Figure 20* show complicated profiles and are quite different from the observed ones in *Figures 13–15*, although the pattern in *Figure 17d* calculated for an undrawn film is similar to the observed ones in *Figures 11a* and *11b*. The disagreement between the observed and calculated patterns indicates that the deformation mechanism of rods is too complicated to represent the scattered intensity mathematically on the basis of the schematic diagram in *Figure 16*. To explain the disagreement, we can propose a model concerning the deformation mechanism of rods shown in *Figure 21*.

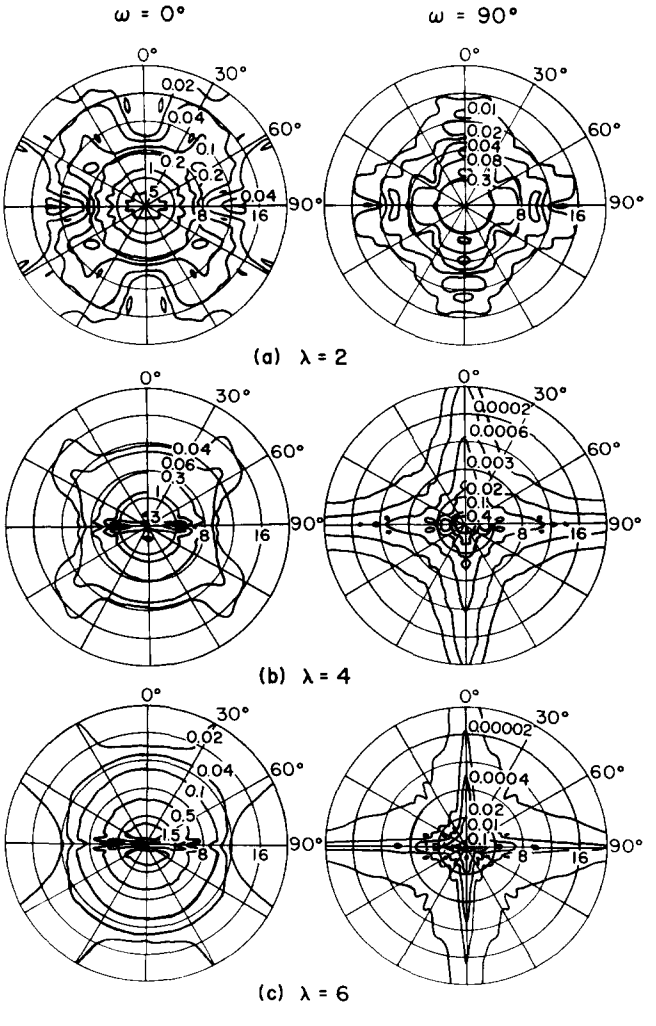

Figure 20 Hv light scattering patterns as a function of draw ratio, in which parameters are fixed at $p = 0.8$, $q = 1$, $\sigma_G/\bar{G} = \sigma_D/\bar{D} = 0.01$, $\sigma_X/\bar{X} = 0.5$ and $\bar{G}/\lambda = 40$

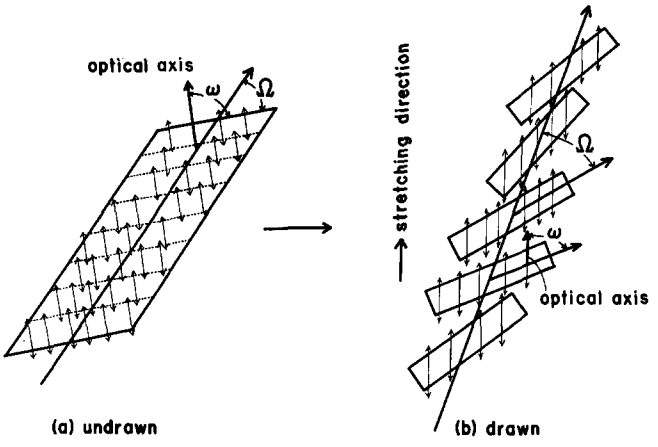

Figure 21 A model representing the orientational behaviour of rods

In this model system, the schematic diagram (a) shows the rods within the film after evaporating solvent, which corresponds to the diagram in *Figure 18b*. *Figure 21b* shows the rods after elongation. With increasing draw ratio λ, the assembly was decomposed into several rods by the tension, and the distance between rods becomes longer. This phenomenon causes interparticle interference effects due to the increase in the ordered arrangement of the rods. However, it is evident that the effects are much more effective than those calculated from the model system in *Figure 16*. Further consideration must be given to represent the significant effects. The separation of rods from the assembly is more significant for specimens A and B than for specimen C because of an increase in strain of tie molecules and/or entanglement meshes with decreasing molecular weight. This concept supports the fact that the drastic change of scattering pattern from +-type to ×-type shifts to higher draw ratio from $\lambda = 1.5$ to 2.0 as shown in *Figures 13–15* and the tensile strength at the same draw ratio decreases as molecular weight increases as shown in *Figure 5*.

CONCLUSIONS

The morphology and mechanical properties of drawn HPC films are dependent upon molecular weight. The drawability becomes more pronounced with increasing molecular weight. The maximum draw ratio of specimen A ($\bar{M}_w = 11.7 \times 10^4$) and B ($\bar{M}_w = 19.2 \times 10^4$) was less than 2.5 and 4.0, respectively, while that of specimen C ($\bar{M}_w = 119.5 \times 10^4$) reached 7. However, the increase in tensile strength at each draw ratio $\leqslant 2.0$ becomes more pronounced with decreasing molecular weight. The storage modulus of specimen C with $\lambda = 6$ was about 7 GPa, but this value is much lower than the crystal lattice modulus of HPC (25 GPa). The storage modulus decreased with temperature, while the crystal lattice modulus is independent of temperature. In spite of the decrease in the storage modulus, the growth of crystallites with temperature was confirmed by X-ray diffraction measurement, which was quite different from the temperature dependence of crystallinity of ultradrawn polyethylene and polypropylene films. The decrease in the Young's (storage) modulus was found to be due to thermal expansion of the average distance between amorphous chain segments.

The light scattering pattern is sensitive to molecular weight. The pattern of specimen B shows +-type lobes at small angles and ×-type at large angles, reflecting interparticle interference effects of rods during the evaporation of solvent, but the ×-type lobes disappeared when the solvent was completely evaporated. However, such behaviour could not be observed for specimen C and the pattern shows only +-type lobes. The patterns observed from the drawn films again showed a profile reflecting interparticle interference effects of rods. This is thought to be due to the separation of rods from the assembly owing to an increase in strain added to tie molecules and/or entanglements.

ACKNOWLEDGEMENT

We are indebted to Dr S. Sudo, Faculty of Engineering, Yamagata University, for valuable discussions and suggestions. We also thank him for measuring molar substitution (MS), weight-average molecular weight ($\bar{M}_w$) and number-average molecular weight ($\bar{M}_n$).

REFERENCES

1 Samuels, R. J. *J. Polym. Sci. (A-2)* 1969, **7**, 1197
2 Wirick, M. G. and Waldman, M. H. *J. Appl. Polym. Sci.* 1970, **14**, 579
3 Smith, P. and Lemstra, P. J. *J. Mater. Sci.* 1980, **15**, 505
4 Smith, P., Lemstra, P. J. and Booij, H. C. *J. Polym. Sci., Polym. Phys. Edn* 1981, **19**, 877
5 Smith, P., Lemstra, P. J., Pijper, J. P. L. and Kiel, A. M. *Colloid Polym. Sci.* 1981, **259**, 1070
6 Andrews, J. M. and Ward, I. M. *J. Mater. Sci.* 1970, **5**, 411
7 Clements, J., Capaccio, G. and Ward, I. M. *J. Polym. Sci., Polym. Phys. Edn* 1979, **17**, 693
8 Kogima, S. and Porter, R. S. *J. Polym. Sci., Polym. Phys. Edn* 1978, **16**, 1729
9 Kang, S. J. and Matsuo, M. *Polym. J.* 1989, **21**, 49
10 Matsuo, M., Sawatari, C. and Ohhata, T. *Macromolecules* 1988, **21**, 1317
11 Matsuo, M. and Sawatari, C. *Macromolecules* 1986, **19**, 2036
12 Matsuo, M. and Sawatari, C. *Macromolecules* 1988, **21**, 1653
13 Sawatari, C. and Matsuo, M. *Macromolecules* 1989, **22**, 2968
14 Gardner, K. H. and Blackwell, J. *Biopolymers* 1974, **13**, 1975
15 Kolpacak, F. J. and Blackwell, J. *Macromolecules* 1976, **9**, 273
16 Matsuo, M., Sawatari, C., Iwai, Y. and Ozaki, F. *Macromolecules* 1990, **23**, 3266
17 Sawatari, C. and Matsuo, M. *Polymer* 1989, **30**, 1603
18 Hashimoto, T., Ebisu, S. and Kawai, H. *J. Polym. Sci., Polym. Phys. Edn* 1981, **19**, 59
19 Rhodes, M. B. and Stein, R. S. *J. Polym. Sci. (A-2)* 1969, **7**, 1539
20 Hayashi, N., Murakami, Y., Moritani, M., Hashimoto, T. and Kawai, H. *Polym. J.* 1973, **4**, 560
21 Blundell, D. J. *Acta Crystallogr. (A)* 1970, **26**, 472
22 Sawatari, C., Iida, M. and Matsuo, M. *Macromolecules* 1984, **17**, 1765